RADAR IMAGE OF ONE DIMENSION ROUGH SURFACE WITH BURIED OBJECT

W.-J. Ji[*] and C.-M. Tong

Missile Institute, Air Force Engineering University, P. O. Box 25, Sanyuan, Shannxi 713800, China

Abstract—In order to detect a buried object quickly and accurately, a fast radar imaging method is presented in this paper. At first, complex backscatter data are computed by using propagation-inside-layer expansion combining the forward and backward method (PILE + FB). Then, a conventional synthetic aperture radar (SAR) imaging procedure called back projection method is used to generate 2-D image. The random rough surface with Gauss spectrum is used to simulate the ground. Tapered incident wave is chosen to reduce truncation error. Because backscatter data are computed by fast numerical method, this method is proper for rough surface with any parameters with a buried complex object, which is very useful for realistic object detection.

1. INTRODUCTION

Due to its important application in military and civilian areas such as the detection of subsurface pipes, landmines and archaeology, the research on electromagnetic sensing of buried objects in the presence of random rough surface has attracted extensive attention. Some approximate analytical models have been derived in small roughness limit problem [1, 2]. However, complexity of the problem has limited the development of more general approximations. In contrast to the approximate analytical methods, numerical methods have many advantages and are not restricted by parameters of rough surface and object. Some works have explored numerical solutions [3–9], and the electromagnetic scattering of 2-D cylinder buried in 1-D randomly soil rough surface is studied by using method of moment (MoM). In [4], a fast numerical method called PILE + FB method is presented to compute the 1-D dielectric rough surface with buried object.

* Corresponding author: Wei-Jie Ji (jiweijie01@163.com).

The detection of buried objects using electromagnetic waves is often obscured by clutters from the rough ground surface. In order to detect the buried object's size and location quickly and accurately, other technologies have been studied. For example, the angular correlation function (ACF) of rough surface with buried object is studied in [10–13]. ACF is the cross correlation function of two scattered fields in different directions θ_{s1} and θ_{s2} corresponding to two distinct incident waves in the θ_{i1} and θ_{i2} directions, respectively. The researches have shown that, in comparison with radar cross section (RCS), by making use of the ACF, the contribution of clutter to the angular correlation function is minimal away from the memory line making the contribution of the buried object more conspicuous by many dB.

All the methods above only study the electromagnetic scattering of rough surface with buried object corresponding to single incidence frequency, which cannot provide elaborate data for the detection of buried object. Thus it is necessary to study this problem from other aspects, such as SAR imaging. Imaging techniques have been widely used in other areas of electromagnetic as a tool for analysis and understanding of scattering and propagation phenomena. For example, studies of natural target scattering have used high-resolution radar images to examine small foliage targets [14–16]. The one dimensional rough surface scattering theories are investigated through analysis of radar images in [17, 18]. In [19], a novel SAR imaging technology is used to target recognition. The requirements of tomographic processing are compounded by the need for data at multiple frequencies and aspect angles. Because of the computing facilities and recent development of efficient numerical methods for backscatter predictions (such as PILE + FB), the back projection formation with numerical scattering models can be realized quickly and accurately. By studying the techniques of the SAR imaging, more information can be provided for the mutual effect between the buried object and rough ground surface, which can provide theory support for detecting technology of buried object.

In this paper, the boundary integral equations of 1-D rough surface with buried perfectly electric conducting (PEC) object are derived based on Huygens surface equivalence principle. And the process of the PILE + FB method is introduced to solve the equations. The backscattering data can be calculated by using this method quickly and correctly. Then, the tomographic processing called back projection is presented to get SAR image by combining the backscattering data calculated by using PILE + FB. To reduce the side-lobe level, several window functions are introduced. Random surface with Gauss
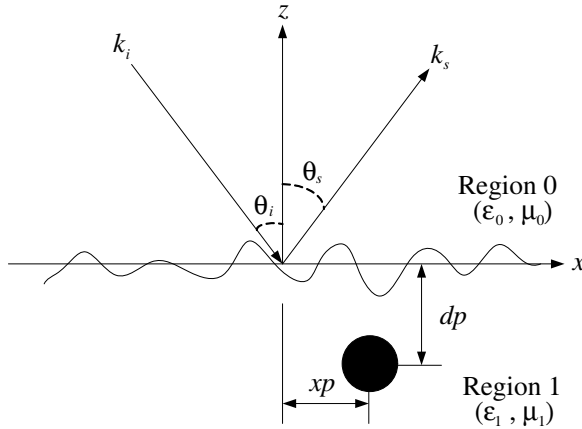
Figure 1. The geometry of a PEC object buried under rough surface.

spectrum is used to simulate the realistic ground. At last, the SAR images of an infinite 2-D cylinder buried under rough ground are computed, and some discussions are made.

2. THEORY AND FORMULATION

2.1. The Boundary Integral Equations

The geometry of a 2-D cylinder buried in 1-D rough surface is shown in Figure 1. The rough surface described by $z = f(x)$ separates the space into upper and down parts. The upper medium is vacuum with parameters ε_0 and μ_0, and the parameters of lower medium are ε_1 and μ_1. $\mathbf{k}_i$ and $\mathbf{k}_s$ are the incidence and scatter direction vectors. θ_i is the incidence angle and θ_s the scattering angle. xp denotes the level distance between the center of object and origin, and dp is the buried depth of object. Let ψ_0 and ψ_1 be the fields in region 0 and region 1, respectively. Let $\mathbf{r}' = x'\hat{\mathbf{x}} + z'\hat{\mathbf{z}}$ and $\mathbf{r} = x\hat{\mathbf{x}} + z\hat{\mathbf{z}}$ denote source and field point, respectively. According to the Huygens surface equivalence principle, we can obtain the following three coupled integral equations for transverse electric field (TE incidence wave):

$$\frac{1}{2}\psi_0(\mathbf{r}) = \psi^{inc}(\mathbf{r}) + \int_{S_r}\left[\psi_0\frac{\partial G_0(\mathbf{r},\mathbf{r}')}{\partial\mathbf{n}} - G_0(\mathbf{r},\mathbf{r}')\frac{\partial\psi_0(\mathbf{r}')}{\partial\mathbf{n}'}\right]ds'$$

$$(\mathbf{r} \in S_r) \qquad (1a)$$

$$\frac{1}{2}\psi_1(\mathbf{r}) = -\int_{S_r}\left[\psi_1(\mathbf{r})\frac{\partial G_1(\mathbf{r},\mathbf{r}')}{\partial \mathbf{n}'} - G_1(\mathbf{r},\mathbf{r}')\frac{\partial \psi_1(\mathbf{r}')}{\partial \mathbf{n}'}\right]ds'$$
$$-\int_{S_0}G_1(\mathbf{r},\mathbf{r}')\frac{\partial \psi_1(\mathbf{r}')}{\partial \mathbf{n}'}ds' \quad (\mathbf{r}\in S_r) \tag{1b}$$

$$\frac{1}{2}\psi_1(\mathbf{r}) = -\int_{S_r}\left[\psi_1(\mathbf{r})\frac{\partial G_1(\mathbf{r},\mathbf{r}')}{\partial \mathbf{n}'} - G_1(\mathbf{r},\mathbf{r}')\frac{\partial \psi_1(\mathbf{r}')}{\partial \mathbf{n}'}\right]ds'$$
$$-\int_{S_0}G_1(\mathbf{r},\mathbf{r}')\frac{\partial \psi_1(\mathbf{r}')}{\partial \mathbf{n}'}ds' \quad (\mathbf{r}\in S_0) \tag{1c}$$

where, S_r and S_0 denote the surface contour of rough surface and object, respectively. ψ^{inc} denotes the incidence field. $G_0(\mathbf{r},\mathbf{r}')$ and $G_1(\mathbf{r},\mathbf{r}')$ are Green's functions in region 0 and region 1. $G_i(\mathbf{r}-\mathbf{r}') = \frac{i}{4}H_0^{(1)}(k_i|\mathbf{r}-\mathbf{r}'|)$ $(i=0,1)$, $H_0^{(1)}$ is the zeroth-order Hankel function of the first kind. k_0 and k_1 are the wave numbers in medium 0 and medium 1. For transverse magnetic field (TM incidence wave), $\int_{S_0}G_1(\mathbf{r},\mathbf{r}')\frac{\partial \psi_1(\mathbf{r}')}{\partial \mathbf{n}'}ds'$ in Equations (1b) and (1c) should be replaced by $\int_{S_0}\psi_1(\mathbf{r})\frac{\partial G_1(\mathbf{r},\mathbf{r}')}{\partial \mathbf{n}'}ds'$.

The boundary condition on the rough surface S_r is:

$$\psi_0(\mathbf{r})|_{\mathbf{r}\in S_r} = \psi_1(\mathbf{r})|_{\mathbf{r}\in S_r} \tag{2a}$$

$$\left.\frac{\partial \psi_0(\mathbf{r})}{\partial \mathbf{n}}\right|_{\mathbf{r}\in S_r} = \frac{1}{\rho}\left.\frac{\partial \psi_1(\mathbf{r})}{\partial \mathbf{n}}\right|_{\mathbf{r}\in S_r} \tag{2b}$$

with $\rho = \mu_1/\mu_0$ for TE incidence, and $\rho = \varepsilon_1/\varepsilon_0$ for TM incidence.

To avoid artificial edge diffraction, the tapered plane wave developed by Thorsos is used, which can be expressed as ([20])

$$\psi^{inc}(\mathbf{r}) = \exp\left[ik(x\sin\theta_i - z\cos\theta_i)\cdot(1 + w(x,z))\right]$$
$$\cdot\exp\left[-\frac{(x + z\tan\theta_i)^2}{g^2}\right] \tag{3}$$

$$w(x,z) = \frac{1}{(k_o g\cos\theta_i)^2}\left[2\frac{(x + z\tan\theta_i)^2}{g^2} - 1\right] \tag{4}$$

where θ_i is the incident angle defined with respect to the normal in the counter-clockwise direction, and g is the tapering parameter with the dimension of length and controls the tapering of the incident wave.

2.2. The PILE + FB Method

The integral equations of rough surface and object are discretized by using MoM with pulse base function. We can obtain the following

matrix equation

$$\mathbf{ZI} = \mathbf{V} \tag{5}$$

where $\mathbf{Z}$ is the total impedance matrix of size $(N + M) \times (N + M)$ (N is the unknown number of rough surfaces, and M is the unknown number of objects). $\mathbf{I}$ is the unknown vector.

$$\mathbf{I}^T = \begin{bmatrix} \mathbf{I}_r^T \mathbf{I}_o^T \end{bmatrix} \tag{6}$$

$\cdot^T$ denotes the transpose operator. $\mathbf{I}_r^T$ is the unknown vector of rough surface and $\mathbf{I}_o^T$ the unknown vector of object.

$\mathbf{V}$ is the incidence field vector.

$$\mathbf{V}^T = \begin{bmatrix} \mathbf{V}_r^T \mathbf{V}_o^T \end{bmatrix} \tag{7}$$

$\mathbf{V}_r^T$ and $\mathbf{V}_o^T$ are the incidence field vectors of rough surface and object, respectively. Because the object is buried under the rough surface, we have $\mathbf{V}_o^T = 0$.

IIn ordertosolvethelinearequation (5)effectively, the impedance matrix is expressed from sub-matrices as

$$\mathbf{Z} = \begin{bmatrix} \mathbf{Z}^r & \mathbf{Z}^{o \to r} \\ \mathbf{Z}^{r \to o} & \mathbf{Z}^o \end{bmatrix} \tag{8}$$

$\mathbf{Z}^r$ and $\mathbf{Z}^o$ correspond to the self-impedance matrices of rough surface and object. The matrices $\mathbf{Z}^{o \to r}$ and $\mathbf{Z}^{r \to o}$ can be interpreted as coupling impedance matrices between object and upper surface.

Define the characteristic matrix $\mathbf{M}_c$ as

$$\mathbf{M}_c = (\mathbf{Z}^r)^{-1} \mathbf{Z}^{o \to r} (\mathbf{Z}^o)^{-1} \mathbf{Z}^{r \to o} \tag{9}$$

The total unknown vector on the rough surface is then be expressed as

$$\mathbf{I}_r = \left[\sum_{p=0}^{p=p_{\text{PILE}}} \mathbf{M}_c^p \right] (\mathbf{Z}^r)^{-1} \mathbf{V}_r = \sum_{p=0}^{p=p_{\text{PILE}}} \mathbf{Y}_r^{(p)} \tag{10}$$

where, p is the step number.

$$\begin{cases} \mathbf{Y}_r^{(0)} = (\mathbf{Z}^r)^{-1} \mathbf{V}_r & \text{for} \quad p = 0 \\ \mathbf{Y}_r^{(p)} = \mathbf{M}_c \mathbf{Y}_r^{(p-1)} & \text{for} \quad p > 0 \end{cases} \tag{11}$$

We define the norm $\|\mathbf{M}_c\|$ of a complex matrix by its spectral radius, i.e., the modulus of its eigenvalue which has the highest modulus. Expansion (10) is accurate if $\|\mathbf{M}_c\|$ is inferior to 1. The physical interpretation of $\mathbf{M}_c$ and derivation process form Equations (8) to (14) are shown in [4].

Upon solving Equations (10) and (11), we can obtain the field ψ_r and $\frac{\partial \psi_r}{\partial n}$ on the rough surface. And the scattering field in upper medium can be calculated as following:

$$\psi_s(\mathbf{r}) = \frac{e^{ik_0 r}}{\sqrt{r}} \psi_s^N(\theta_s, \theta_i) \tag{12}$$

with

$$\psi_s^N(\theta_s, \theta_i) = \frac{i}{4}\sqrt{\frac{2}{\pi k_0}} e^{-i\frac{\pi}{4}} \int_{S_r} \left[-i(\hat{\mathbf{n}} \cdot \mathbf{k}_s)\psi_r(x) - \frac{\partial \psi_r(x)}{\partial n} \right] e^{-i\mathbf{k}_s \cdot \mathbf{r}} ds \tag{13}$$

where, $\mathbf{k}_s = k_0(\sin\theta_s \hat{\mathbf{x}} + \cos\theta_s \hat{\mathbf{z}})$, θ_s is the scattering angle.

The expression for the normalized scattering coefficient with tapered plane wave incidence is given by

$$\sigma(\theta_s) = \frac{\left| \psi_s^N(\theta_s, \theta_i) \right|^2}{g\sqrt{\pi/2} \cos\theta_i \left(1 - \frac{1+2\tan^2\theta_i}{2k_0^2 g^2 \cos^2\theta_i} \right)} \tag{14}$$

2.3. The Back Projection Algorithm

A brief description of the tomographic processing is given below. A radar image of a target is obtained using the target-scattered fields over a given frequency band and aspect region. The scattered field data are available over $f_{\min}$ to $f_{\max}$ frequency band and θ_1 to θ_2 angle band by using the method introduced in sections 2.1 and 2.2. Then, a radar image of the target is obtained from

$$I(x, z) = \int_{\theta_1}^{\theta_2} \int_{f_{\min}}^{f_{\max}} G(f, \theta) q(f) q(\theta) e^{-i2\pi f t(\theta)} f df d\theta \tag{15}$$

where, $G(f, \theta)$ is the complex backscatter data in the frequency and angle domains, and $q(f)$ and $q(\theta)$ are weighting functions for frequency and aspect, respectively. The function $t(\theta)$ is given by

$$t(\theta) = \frac{2(x\sin\theta - z\cos\theta)}{c} \tag{16}$$

where, c is the velocity of light. The relationship among x, z and θ is shown in Figure 2.

The weighting functions are normalized so that [17]

$$\int f q(f) df = \int q(\theta) d\theta = 1 \tag{17}$$

By rewriting Equation (15), we obtain

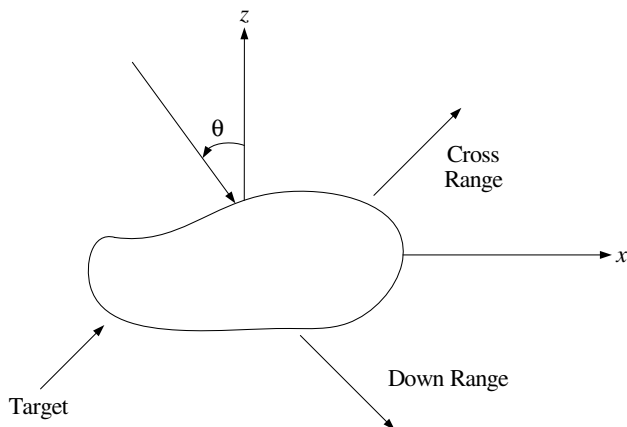$$I(x, z) = \int_{\theta_1}^{\theta_2} J(\theta) q(\theta) d\theta \tag{18}$$

Figure 2. Imaging geometry for a target.

where

$$J(\theta) = \int\limits_{f_{\min}}^{f_{\max}} G'(f,\theta)e^{-i2\pi ft(\theta)}df \tag{19}$$

With

$$G'(f,\theta) = fG(f,\theta)w(f) \tag{20}$$

Equation (19) takes the form of a Fourier transform. Therefore, if the scattered field data are obtained with uniform frequency increments, Equation (19) can be evaluated using an IFFT. Then, $J(\theta)$ is used in Equation (18) to obtain the complex value of $I(x,z)$.

Since radar data are measured at discrete frequencies and aspect angles, the integrals in Equation (15) can be approximated as summations. The radar image is then given by

$$I(x,z) = \sum_{m=1}^{M} \sum_{n=N_1}^{N_2} (n\Delta f)G(n\Delta f,\theta_m)q(n\Delta f)$$
$$\cdot q(\theta_m)e^{-i\frac{4\pi}{c}n\Delta f(x\sin\theta_m - z\cos\theta_m)} \tag{21}$$

where Δf is the frequency increment. $N_1 = f_{\min}/\Delta f$, $N_2 = f_{\max}/\Delta f$. The more aspect angles are available to reconstruct the image with a given bandwidth, the better quality is the resulting image.

Down- and cross-range resolutions of the image can be determined by the frequency and angular bandwidth, respectively. The down-

range and cross-range resolutions, r_d and r_c, are given by [17]

$$r_d = \frac{c}{2B} \quad r_c = \frac{c}{2f_0 \sin \Theta} \tag{22}$$

B and Θ represent the frequency bandwidth centered on f_0 and the angular rotation, respectively. c is the velocity of light. To resolve surface variations on the order of a wavelength, backscatter data are typically collected over $4\,\text{GHz}$ frequency bandwidth ($3 \sim 7\,\text{GHz}$) and a $40°$ angular bandwidth corresponding $3.75\,\text{cm}$ down- and $4.67\,\text{cm}$ cross-range resolution in the image domain, respectively.

The unambiguous down- and cross-ranges, D_d and D_c, can be obtained by the following equations:

$$D_d = \frac{c}{2\delta_f} \quad D_c = \frac{c}{2f_0\delta_\theta} \tag{23}$$

where, δ_f and δ_θ denote the steps in frequency and angle, respectively. Step sizes with $100\,\text{MHz}$ ($D_d = 1.5\,\text{m}$) frequency and $0.2°$ ($D_c = 8.6\,\text{m}$ at $f_0 = 5\,\text{GHz}$) angle steps are typically used so that image formation with large down-range and cross-range unambiguous regions are possible at normal incidence.

To reduce the side-lobe level, a proper choice of windows for frequency and angle is necessary. Several well-known window functions are used in this paper [21].

Rectangular Window:

$$W(n) = 1 \quad n = 0, 1, \ldots, N-1 \tag{24}$$

Hamming Window:

$$W(n) = 0.54 - 0.46 \cos\left(\frac{2\pi n}{N}\right) \quad n = 0, 1, \ldots, N-1 \tag{25}$$

Blackman Window:

$$W(n) = 0.42 - 0.5 \cos\left(\frac{2\pi n}{N}\right) + 0.08 \cos\left(\frac{4\pi n}{N}\right)$$
$$n = 0, 1, \ldots, N-1 \tag{26}$$

3. THE NUMERICAL RESULTS

The random surface with Gauss spectrum is used to simulate the realistic ground in this paper. The Gauss spectrum is given by [20]:

$$W(k_x) = \frac{\sigma^2 l}{2\sqrt{\pi}} e^{-\frac{k_x^2 l^2}{4}} \tag{27}$$

k_x is the spatial spectrum in x direction. σ is the root-mean-square height, and l is the correlation length.

At first, we investigate synthetic aperture radar (SAR) images of the PEC cylinder buried under rough surface as shown in Figure 1. The surface size of the Gauss surface is $L = 1.98$ m (33λ at 5 GHz) with 1024 surface unknowns. The other parameters are: $\sigma = 1.25$ cm, $l = 0.75$ cm. The parameters of object are: radius $R = 0.1$ m, $xp = 0.0$ m, $dp = 0.3$ m. And the number of object's surface unknowns is 120. The relative dielectric permittivity of lower medium is given by $\varepsilon_1 = 4.24 + 0.36i$ (the soil of 5% moisture). Let $f = 3 \sim 7$ GHz, $\delta f = 100$ MHz, $\theta_i = -20° \sim 20°$ and $\delta\theta = 0.2°$. Thus a total 8241
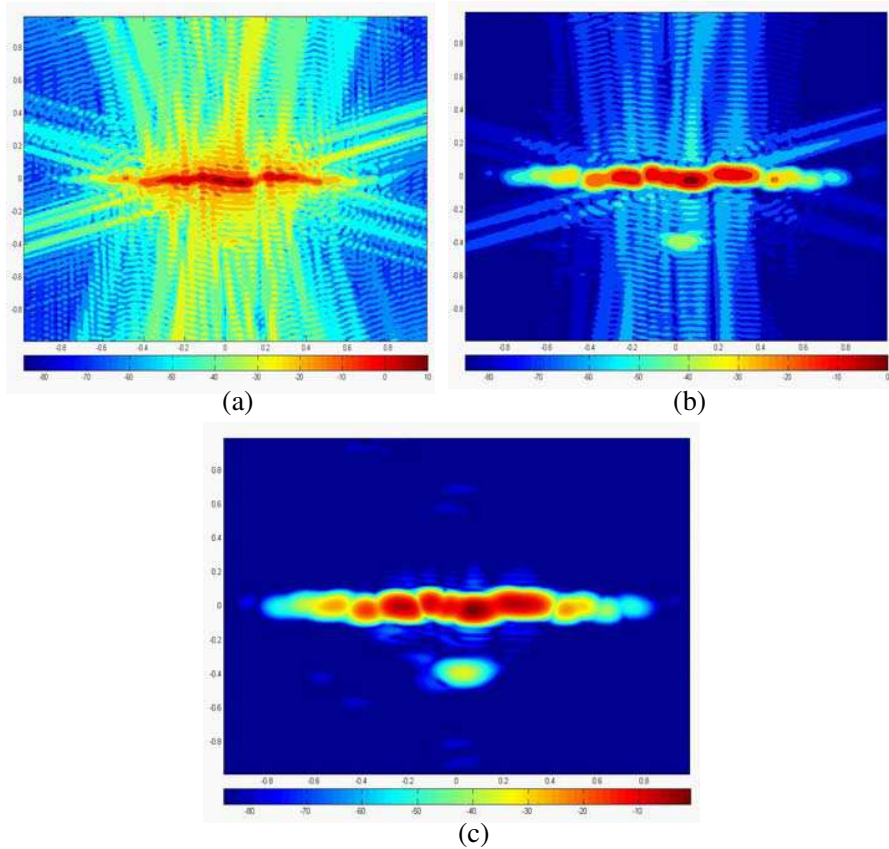

Figure 3. The image of different window functions. (a) Image with rectangular window. (b) Image with Hamming window. (c) Image with Blackman window.

backscattering calculations are required.

Figure 3 demonstrates the effect of the window function for SAR image, and the incidence wave is TE polarization. Each image is expressed with the dynamic range of 85 dB ($-85 \sim 0$ dB) and composed of 200×200 pixels in $2\,\mathrm{m} \times 2\,\mathrm{m}$ range so that each pixel size is much smaller than the range resolution. As expected, image with rectangular window provides the worst resolution. With high first side-lobe (-13 dB) and low peak spectrum asymptotic attenuation speed (-6 dB/oct), the rectangular window is not appropriate for discerning multiple scattering effects due to strong side-lobes. From Figure 3(a), we nearly cannot find the object. The SAR image with Hamming window is better than the one with rectangular window, but is also not enough. The image with low first side-lobe (-58 dB) and high peak spectrum asymptotic attenuation speed (-18 dB/oct) Blackman window demonstrates much improved main-lobe and side-lobe ratio but also reduced resolution. From Figure 3(c), we can clearly see the image of surface and object, and the mutual effect between them can also be found.

As shown in the figure, the target image location deviated from the actual target location because of different dielectric permittivity results in the reduced wave velocity and therefore increased travel time inside the medium. Thus, the target image's location is deeper than the actual target location.

Figure 4 shows the SAR image of buried object for both TM and TE incidence waves, and the Blackman window is used. The images are expressed within the dynamic range of 65 dB ($-65 \sim 0$ dB) and
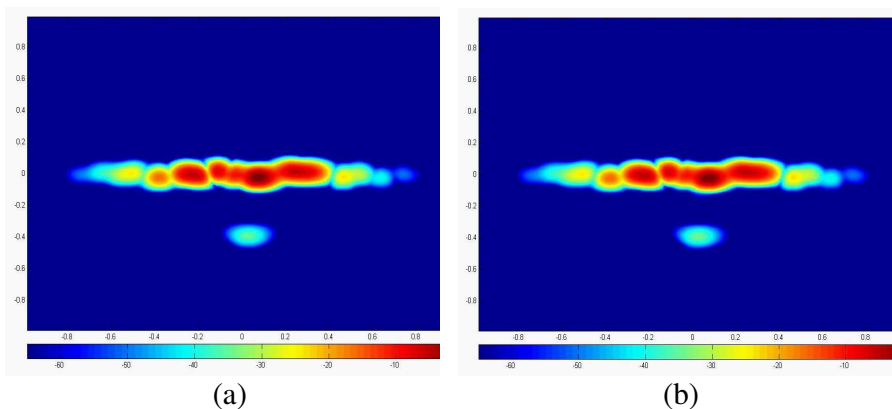

Figure 4. The image of different polar incidence waves. (a) TM. (b) TE.

composed of 200×200 pixels. We can see clearly the SAR image of the ground surface and object. The results show that the method proposed in this paper is appropriate for both TM and TE incidence waves.

Figure 5 shows the SAR image of buried cylinder objects with different sizes and positions, and the incidence wave is TM polarization. The Blackman window is used in all the following results. In Figure 5(a), the position of object is $xp = 0.2 \, \text{m}$, $dp = 0.3 \, \text{m}$. We can observe clearly that the position of the object has already changed compared with Figure 4. Figure 5(b) shows the the image of object with buried depth of $0.2 \, \text{m}$. And we can find that the image of object is clearer than that in Figure 4, partly owing to the increasing mutual
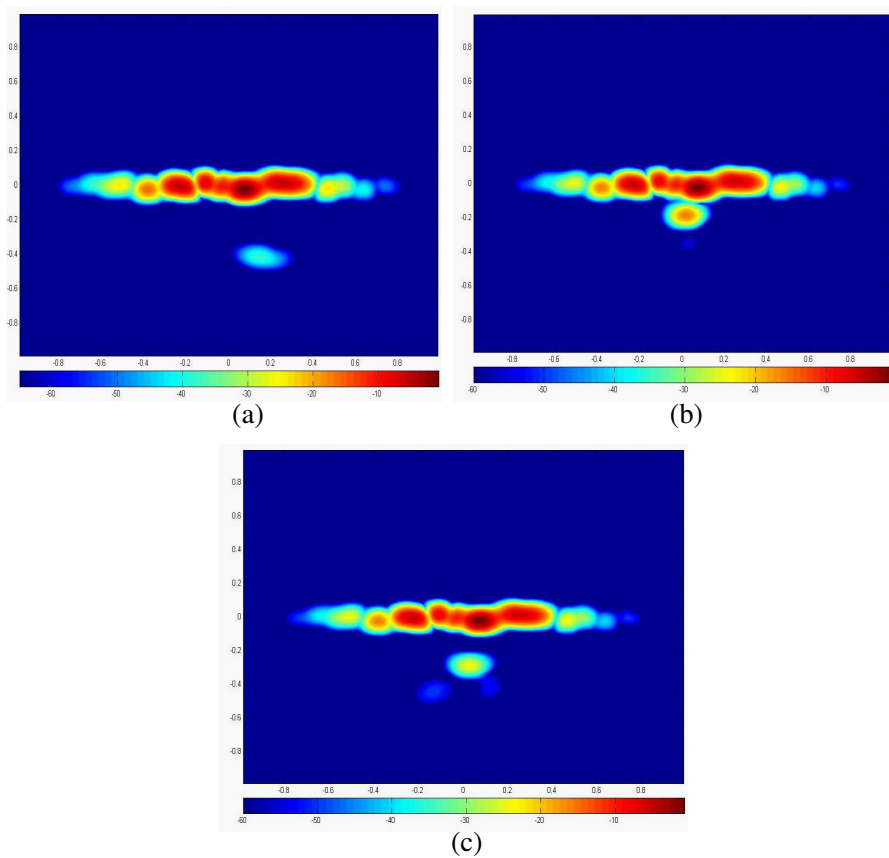

(a)

(b)

(c)

Figure 5. The SAR image of buried objects with different sizes sand positions. (a) $xp = 0.2 \, \text{m}$, $dp = 0.3 \, \text{m}$, $R = 0.1 \, \text{m}$. (b) $xp = 0 \, \text{m}$, $dp = 0.2 \, \text{m}$, $R = 0.1 \, \text{m}$. (c) $xp = 0 \, \text{m}$, $dp = 0.3 \, \text{m}$, $r = 0.15 \, \text{m}$.

effect between object and rough ground. The image of cylinder with radius of 0.15 m can be observed in Figure 5(c). The result shows that the image of object is clearer than that with smaller radius. In other words, the algorithm introduced in this paper can obtain good SAR image of rough surface with buried object.

4. CONCLUSIONS

A two dimensional SAR imaging algorithm for one dimensional rough ground surface with buried object is introduced in this paper. The fast numerical method called PILE + FB is used to calculate the backscattering data, and the SAR image can be computed by using the back projection method. The results show that good image result can be obtained for both TM and TE incidence waves. At the same time, we know that the result is worst when the window function is rectangular window. However, the Blackman window function gets the finest image result. The results also show that good images can be obtained for objects with different sizes and positions. This method provides a very good way to achieve underground target detection and has important application value.

ACKNOWLEDGMENT

REFERENCES

1. Zhang, Y., Y. E. Yang, H. Braunisch, and J. A. Kong, "Electromagnetic wave interaction of conducting object with rough surface by hybrid SPM/MoM technique," *Progress In Electromagnetics Research*, Vol. 22, 315–335, 1999.
2. Ishimaru, A., J. D. Rockway, and Y. Kuga, "Rough surface Green's function based on the first-order modified perturbation and smoothed diagram methods," *Waves Random Media*, Vol. 10, 17–31, 2000.
3. Wang, R., L.-X. Guo, and A.-Q. Wang, "Investigation of electromagnetic scattering interaction between the buried and the

rough surface in different types of soil," *Chinese Physics*, Vol. 59, No. 8, 3179–3186, 2010.

4. Bourlier, C., G. Kubické, and N. Déechamps, "A fast method to compute scattering by a buried object under a randomly rough surface: PILE combined to FB-SA," *J. Opt. Soc. Amer. A*, Vol. 25, 891–902, 2008.

5. Wang, X., C.-F. Wang, Y.-B. Gan, and L.-W. Li, "Electromagnetic scattering from a circular target above or below rough surface," *Progress In Electromagnetics Research*, Vol. 40, 207–227, 2003.

6. Johnson, J. T. and R. J. Burkholder, "A study of scattering from an object below a rough surface," *IEEE Trans. Geosci. Remote Sensing*, Vol. 42, 59–66, 2004.

7. El-Shenawee, M., C. M. Rappaport, E. L. Miller, and M. B. Silevitch, "Three-dimensional subsurface analysis of electromagnetic scattering from penetrable/PEC objects buried under rough surfaces: Use of the steepest descent fast multipole method," *IEEE Trans. Geosci. Remote Sensing*, Vol. 39, 1174–1182, 2001.

8. Ji, W.-J. and C.-M. Tong, "The E-PILE + SMCG for scattering form an Object below 2D soil rough surface," *Progress In Electromagnetics Research B*, Vol. 33, 317–337, 2011.

9. Ji, W.-J. and C.-M. Tong, "Bistatic scattering from two-dimensional dielectric ocean rough surface with a PEC object partially embedded by using the G-SMCG method," *Progress In Electromagnetics Research*, Vol. 105, 119–139, 2010.

10. Kuga, Y., C. T. C. Le, A. Ishimaru, and L. Aies-Sengers, "Analytical, experimental and numerical studies of angular memory signatures of waves scattered from one-dimensional rough surfaces," *IEEE Trans. Geosci. Remote Sensing*, Vol. 34, 1300–1307, 1996.

11. Michel, T. R. and K. A. O'Donnell, "Angular correlation functions of amplitudes scattered from a one-dimensional, perfectly conducting rough surface," *J. Opt. Soc. Amer. A*, Vol. 9, No. 8, 1374–1384, 1992.

12. Zhang, G., L. Tsang, and Y. Kuga, "Studies of angular correlation function of scattering by random rough surfaces with and without a buried object," *IEEE Trans. Geosci. Remote Sensing*, Vol. 35, 444–453, 1997.

13. Zhang, G., L. Tsang, and K. Pak, "Angular correlation function and scattering coefficient of electromagnetic waves scattered by a buried object under a two-dimensional rough surface," *J. Opt.*

Soc. Amer. A, 2995–3002, Dec. 1998.

14. Fortuny, J. and A. J. Sieber, "Three-dimensional synthetic aperture radar imaging of a fir tree: First results," *IEEE Trans. Geosci. Remote Sensing*, Vol. 37, 1006–1014, Mar. 1999.

15. Kim, H., J. T. Johnson, and B. Baertlein, "High resolution Ka-band backscatter images of a small tree: Measurements and models," *IEEE Trans. Geosci. Remote Sensing*, 899–910, Mar. 2000.

16. Brown, S. and J. C. Bennett, "High-resolution microwave polarimetric imaging of small trees," *IEEE Trans. Geosci. Remote Sensing*, Vol. 37, 48–53, Jan. 1999.

17. Kim, H. and J. T. Johnson, "Radar images of rough surface scattering: Comparison of numerical and analytical models," *IEEE Trans. Antennas and Propagation*, Vol. 50, No. 2, 94–100, 2002.

18. Kim, H. and J. T. Johnson, "Radar image studies of an ocean-like surface," *Microwave and Optical Technology Letters*, Vol. 30, No. 9, 381–384, 2001.

19. Chang, Y.-L., C.-Y. Chiang, and K.-S. Chen, "SAR image simulation with application to target recognition," *Progress In Electromagnetics Research*, Vol. 119, 35–57, 2011.

20. Thorsos, A., "The validity of the Kirchhoff approximation for rough surface scattering using a Guassian roughness spectrum," *Journal of the Acoustical Society of America*, Vol. 83, No. 1, 78–92, 1988.

21. Harris, F. J., "On the use of windows for harmonic analysis with the discrete Fourier transform," *Proc. IEEE*, Vol. 66, 55–58, Jan. 1978.